Tectonophysics 856 (2023) 229857

Contents lists available at ScienceDirect

Tectonophysics

journal homepage: www.elsevier.com/locate/tecto

The electrical conductivity of granite: The role of hydrous accessory minerals and the structure water in major minerals

Kui Han [a,b], Xinzhuan Guo [c,d,*], Xuben Wang [a], Junfeng Zhang [c], Sinan Özaydin [b], Dewei Li [e], Simon Martin Clark [b]

[a] Kay Laboratory of Earth Exploration and Information Techniques (Chengdu University of Technology), Ministry of Education, Chengdu, Sichuan 610059, China
[b] ARC Centre of Excellence for Core to Crust Fluid Systems & School of Natural Sciences, Macquarie University, Sydney, NSW 2109, Australia
[c] State Key Laboratory of Geological Processes and Mineral Resources, China University of Geosciences, Wuhan, Hubei 430074, China
[d] CAS Key Laboratory of High-Temperature and High-Pressure Study of the Earth' Interior, Institute of Geochemistry, Chinese Academy of Sciences, Guiyang, China
[e] Chengdu Center of China Geological Survey, Chengdu 610081, China

ARTICLE INFO

Keywords:
Electrical conductivity
Granitoid
Continental crust
Dehydration melt
Feldspars

ABSTRACT

The electrical conductivity of granitic rocks (granitoids) is crucial to understand the rock composition, physiochemical state and structure of the crust. However, it is not clear how the conductivity of granitoids is affected by the incorporated water in major minerals and hydrous accessory minerals. Here, we measured the electrical conductivity of two natural granites and two synthetic aggregates compositionally similar to the granites at temperatures of 573–1273 K and pressures of either ambient pressure or 1 GPa. No mineral preferred orientation was observed for the natural samples. The hydrous accessory minerals in the samples, including muscovite, biotite and amphibole, start to dehydrate at about 700 K at ambient pressure, but barely affect the bulk conductivity. The increase in conductivity of granite by more than half orders of magnitude at 1273 K and 1GPa indicated the onset of melting due to the dehydration of biotite. The conductivities of synthetic aggregates are higher than the granite samples, suggesting that the structural water in feldspars could influence, to a moderate degree, the conductivity of granite. We combined the effect of modal composition and structural water on the conductivity of granite and derived a maximal electrical conductivity of a granitoid at different geological settings. The maximal conductivity can be 0.004 ± 0.0001 S/m at 60 km under orogens, over one order of magnitude higher than a cratonic crust. The maximal conductivity provides an upper limit for interpreting the electrical anomalies in the crust.

1. Introduction

Electrical conductivity of minerals and rocks is an important physical property for determining the composition and architecture of the deep Earth (Özaydın and Selway, 2020; Robertson et al., 2016). High conductivity anomalies in the crust could be caused by several factors, including composition and temperature, structural water in the minerals, the presence of melts, aqueous fluids, hydrous minerals, magnetite, grain boundary graphite films, sulfide minerals or film (Duba et al., 1994; Guo et al., 2018; Guo et al., 2015; Hu et al., 2022; Kawano et al., 2012; Yoshino, 2010; Selway, 2014; Unsworth et al., 2005; Xu et al., 2019). However, the origin of the high conductivity anomalies is still in debate. For example, the presence of partial melts inferred as a plausible candidate is generally corroborated by low seismic velocity, whereas several conductive anomalies in a cratonic crust, such as the conductor beneath the Curnamona Province, Australia, is hard to be explained by partial melt (Robertson et al., 2016). Granite, the most abundant rock in the continental crust, is present in a variety of geological settings; therefore, a better understanding of the electrical conductivity of granite could help constrain the causes of the conductive anomalies (Nédélec and Bouchez, 2015; Parkhomenko, 1982; Dai et al., 2014; Guo et al., 2018) The electrical conductivity of granite is influenced by many factors to a varying degree, such as the temperature, chemical composition, oxygen fugacity, and the presence of free water. The conductivity of granite is considerably controlled by free water (Olhoeft, 1981), whereas the granite in the deep crust is mostly dry. Parkhomenko (1982) reviewed the conductivity of dry granite samples at high temperature and high pressure before then. Shanov et al. (2000) measured the

* Corresponding author at: State Key Laboratory of Geological Processes and Mineral Resources, China University of Geosciences, Wuhan, Hubei 430074, China.
E-mail addresses: hankui@cdut.edu.cn (K. Han), gxzhuan@mail.gyig.ac.cn (X. Guo).

https://doi.org/10.1016/j.tecto.2023.229857
Received 25 November 2022; Received in revised form 20 March 2023; Accepted 7 April 2023
Available online 23 April 2023

conductivity of granite from South Bulgaria at ambient pressure and 820 °C. Most conductivity measurements were conducted using direct current (DC), which failed to exclude the effect of polariton at electrode-sample interface (Yoshino, 2010). AC Impedance spectroscopy has been adopted to measure the conductivity of various granite samples (Guo et al., 2017; Dai et al., 2014). Dai et al. (2014) proposed a quantitative model to calculate the conductivity of dry granite based on the chemical composition. The previous studies focused on dry granite without structural water in the minerals (or even neglected as a source). However, a "dry" granite incorporates stoichiometric water in the hydrous accessory minerals (mica and amphibole) and structural water in the major minerals (feldspars and quartz). Hydrous accessory minerals normally exhibit high electrical conductivity and this could bring about a dramatic increase in rock conductivity if a connected network has been formed (Duba et al., 1994; Dyck et al., 2020). The dehydration or dehydroxylation of hydrous minerals release aqueous fluid leading to an increase in electrical conductivity (Litovchenko and Mazykin, 1984; Saltas et al., 2020; Chen et al., 2018). The dehydration of these accessory minerals not only alters the thermochemical equilibrium and induces dehydration melting (Aranovich et al., 2014), also causes the oxidation of iron (from Fe^{2+} to Fe^{3+}) which enhances the conductivity of a rock (Hu et al., 2018; Wang et al., 2012; Shanov et al., 2000). However, several studies have reported a constant conductivity for granite at the dehydration temperature which prevents one from examining the effect of hydrous accessory minerals on the conductivity of granite (Dai et al., 2014; Parkhomenko, 1982; Olhoeft, 1981). Besides, structural water controls the conductivity of hydrous feldspars and thus could affect the conductivity of granite (Yang, 2012; Yang et al., 2012; Amulele et al., 2022; Hu et al., 2022). Although water in granite prone to be stored in the hydrous accessory minerals during fractionation crystallization, feldspars may incorporate a structural water content of up to 0.1 wt% (Aranovich et al., 2014; Johnson, 2006; Mosenfelder et al., 2015). Thus, there are few studies that examine how structural water in minerals could affect the conductivity of granite. An investigation into the role of water in accessory and major minerals would allow for a comprehensive understanding of the electrical conductivity of granite and its role in underpinning the geoelectric profiles in the crust.

The objective of this study is to clarify the role of water in hydrous accessory and major minerals on the electrical conductivity of granite. To this end, we measured the electrical conductivity of natural and synthetic granite, as well as the constituents at both 1 GPa and ambient pressure and at various temperatures. The information on the structural water content of major minerals along with the chemical composition was integrated into the modeling of the conductivity of granitic rocks (granitoids). This model was then used to identify an upper limit of electrical conductivity of granitoids.

2. Methods

2.1. Sample preparation and characterization

Two natural granite samples, Hartley granite (HG) and Quarry granite (QG), were used to prepare the starting materials. The former is a fresh pink granite, collected from an outcrop at Hartley Village, NSW, Australia. The latter is a pale granite-granodiorite, obtained from the Quarry Park, Rocklin, California, USA, which is in the foothills of the Sierra Nevada. The Hartley and Quarry granites were separately ground to powders (<10 μm) and then cold-pressed to cylindrical samples using a 5% polyvinyl alcohol solution (C_2H_4O) that acts as a chemical adhesive before mechanical compaction. These two samples were labeled as HGNP and QGNP, respectively. The compacted HGNP and QGNP were then heated in an oven at 773 K for around 5 h to evaporate the vinyl alcohol and expel the absorbed water in the pellets. We also directly cored the Hartley and Quarry granites to obtain the cylindrical samples, labeled as HGND and QGND, respectively. Three natural samples, named Qtz-R, Or-R and Ab-R (same as those used in our previous study, Han et al., 2021) were also cored. We machined the HGND, QGND, Qtz-R, Ab-R and Or-R into discs with a diameter of 12 mm and a thickness of 1.5 mm, followed by double-polished to ensure that the two faces were parallel to each other. Then the samples were stored in an oven at 373 K over 24 h to eliminate the absorbed water on the sample surface before the impedance spectroscopy measurements. The Qtz-R, Or-R and Ab-R samples were powdered to <10 μm, and then mixed in two proportions corresponding to the modal composition of Hartley granite and Quarry granite, in order to synthesis two granitic aggregates, HGSP and QGSP, respectively. In other words, the HGSP is composed of 41.7 wt% quartz, 21.6 wt% plagioclase, and 36.7 wt% K-feldspar. The QGSP is made up of 37.7 wt% quartz, 44.5 wt% plagioclase, and 16.9 wt% K-feldspar.

The Hartley granite and The Quarry granite are both mainly composed of quartz, plagioclase and feldspars. Quarry granite has 4.4 wt % of accessory hydrous minerals including mica (biotite and muscovite) and amphibole (Fig. 1 and S1), while only mica was observed in Hartley granite. The grain size of the constitutive minerals was 200–600 μm for the Hartley granite and 400–1200 μm for the Quarry granite. Neither oriented fabrics, fractures nor pores were observed in both granites under a microscope. The chemical composition of the granites and their constitutive minerals were determined by X-ray fluorescence (XRF) and electron microprobe analysis (EMPA), respectively, in the MQ geoanalytical facilities of the Department of Earth and Environmental Sciences (EES), Macquarie University, Sydney, Australia. The EMPA used an accelerating voltage of 15 kV with a current of 20 nA. The beam size was 10 μm. Micro-XRF and point counting were used to determine the modal composition. The granite samples were polished using 0.05 μm colloidal silica before the crystal orientation of the major constituents was identified using electron backscatter diffraction (EBSD). The instrument was equipped with a Horiba IHR320 EBSD detector on a Zeiss EVO MA15 scanning electron microscope platform. An accelerating voltage of 25 kV and a step size of 4.6 μm were used. The Channel 5 software suite was used to process the EBSD data. The preferred crystallographic orientation of the grains was investigated graphically using pole figures in which each point represents one grain (Fig. 2).

HGNP and QGNP were pressed into pellets using a 5% polyvinyl alcohol solution (C_2H_4O) that acts as a chemical adhesive before mechanical compaction. The compacted HGNP and QGNP were then heated in an oven at 773 K for around 5 h to evaporate the vinyl alcohol and expel the absorbed water in the pellets. We machined the HGND, QGND, Qtz-R, Ab-R and Or-R into discs with a diameter of 12 mm and a thickness of 1.5 mm, followed by double-polished to ensure that the two faces were parallel to each other. Then the samples were stored in an oven at 373 K over 24 h to eliminate the absorbed water on the sample surface before the impedance spectroscopy measurements.

For the conductivity measurements at 1 GPa, HGSP, QGSP, QGNP and QGND were used. The HGSP and QGSP were sealed in a Pt capsule, and hot pressed at 1 GPa and 773 K for 3 h and then annealed at 1173 K for 3 h using the modified Griggs deformation apparatus at the State Key Laboratory of Geological Processes and Mineral Resources (SKL-GPMR), China University of Geosciences, Wuhan, China. The detailed configuration of the sample assembly is given by Wang et al. (2012). QGNP, QGND and the hot pressed HGSP and QGSP were machined into cylinders with a diameter of 2 mm a thickness of 1 mm. These machined samples were placed into a MgO sleeve with nickel electrodes at both ends where the nickel also served as an oxygen buffer. Graphite was used in the furnace to generate heat. The sample assembly was hosted by a MgO-Cr_2O_3 doped octahedra of 18 mm truncated edge length (TEL). Platinum/rhodium-10%/platinum wires were used as thermocouples as well as serving as the lead wires for impedance measurements (Li et al., 2018). The prepared sample assemblies were loaded into the Walker-type 1000-ton MAA system at the SKL-GPMR, China University of Geosciences (Wuhan).

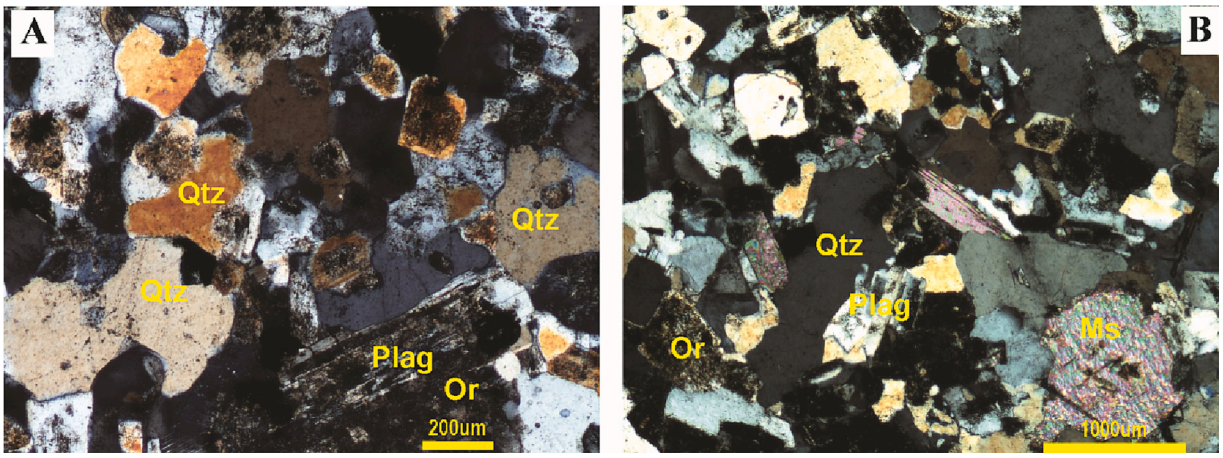

Fig. 1. Photomicrographs of thin sections of the Hartley granite (A) and Quarry granite (B). The alteration for Quarry granite is negligible but it can be observed for Hartley granite. Plag, plagioclase; Qtz, quartz; Or, orthoclase; Ms., muscovite.

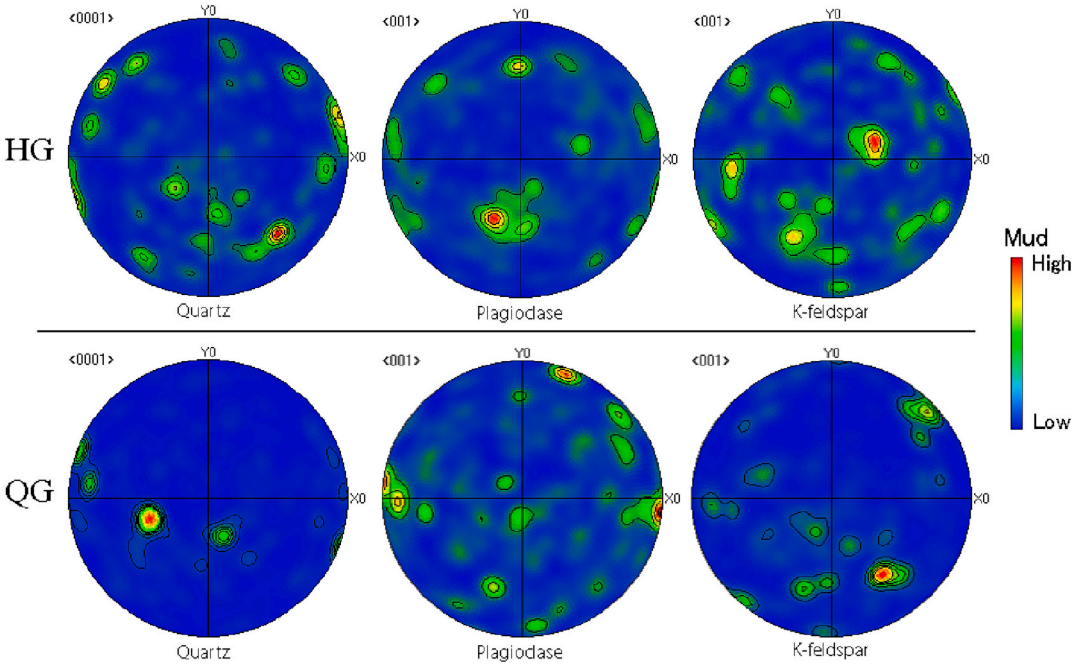

Fig. 2. Contoured pole figures of the *c*-axis orientation of quartz, plagioclase, and K-feldspar in the Hartley granite and Quarry granite based on the electron backscatter diffraction maps. All the pole figures show the projection from the upper hemisphere. Each pole plot is based on >200 mineral grains. Both the half-width and cluster size are 10°. The multiples of uniform distribution (Mud) represent the contour density of the crystallographic orientations.

2.2. Measurement of water content

To examine the dehydration of hydrous accessory minerals, the weight loss of the samples was determined by thermogravimetric analysis (TGA) using a TA Instrument TGA2050 in the Department of Molecular Sciences, Macquarie University. The Hartley and Quarry granite samples were powdered to a grain size of about 10 μm and then heated in platinum (Pt) crucibles. Nitrogen flowing at a rate of 50 cm^3/min was used as the gaseous atmosphere to purge the thermobalance of the gas produced from the samples and to minimize the possibility of the samples from reacting with any water vapor released from the test samples (Bish and Duffy, 1990). The samples were heated from 300 K to 1273 K at a rate of 10 K /min. Differential thermogravimetric analysis (DTG) curves were generated for measurement of the differences in weight as a function of temperature at 1 min intervals. Fourier transform infrared (FTIR) spectroscopy was used to determine the content of structural water in constitutive minerals of the Quarry granite. The FTIR measurements were conducted using a Nicolet 6700 (Thermo Scientific Nicolet continuum infrared microscope), at the State Key Laboratory of Geological Processes and Mineral Resources (SKL-GPMR), China University of Geosciences (Wuhan). The apparatus was equipped with a tungsten light source, a KBr beam splitter, and a mercury-cadmium-telluride (MCT) detector. The illumination aperture was set at a diameter of 100 mm, providing a beam size of 100 × 100 μm on the sample. For each measurement, 128 scans were collected with a resolution of 4 cm^{-1}. We were unable to measure the water content of the major minerals for Hartley granite because of the turbid feldspars related to alteration.

2.3. Impedance spectroscopy measurements

The conductivity measurements at ambient pressure were performed

with an MTZ-35 impedance analyzer at the University of Sydney, Australia, with a voltage of 0.5 V and a frequency range from 0.1 to 107 Hz. The temperature for measurement varied from 473 to 773 K. The conductivity measurements at 1 GPa were performed using a Solartron 1260 impedance gain-phase analyzer based at CUG (Wuhan), China. The impedance data were collected over multiple cycles which included several heating and cooling cycles at low temperature, below 873 K, followed by measurements over several cycles at higher temperatures up to 1273 K. All impedance spectroscopy data at both ambient pressure and 1 GPa were collected with an interval of 50–100 K and 2–3 heating-cooling cycles were performed to check the data reproducibility. The samples were found to be slightly distorted after the measurements, thus the dimensions of the post-experiment samples were measured and used to refine the electrical conductivity. The total error due to the impedance spectroscopy measurements and fitting in Zview was estimated to be <5%.

3. Results

3.1. Physical and chemical properties

The bulk composition of Hartley granite is similar to that of Quarry granite, except that the Hartley granite contains more potassium and less calcium and sodium than Quarry granite (Table 1). The Quarry granite contains more plagioclase and accessory minerals but less K-feldspar than Hartley granite (Table 2). The chemical compositions of these major minerals were similar between the two granites. The *c* axis orientations of the quartz (⟨0001⟩), plagioclase (⟨001⟩), and K-feldspar (<001>) in both granites are plotted as pole figures in Fig. 2. These minerals in both the Hartley granite and the Quarry granite show a weak preferred orientation, although the quartz in the Quarry granite was slightly oriented.

The TGA curves in Fig. 3 show the weight change of the two granite samples as the temperature is increased, while the DTG curves reveal the ratio of the weight loss. The stable weight loss of the Hartley granite below 688 K and the Quarry granite below 723 K may be attributed to the loss of water that was physically absorbed on the mineral grain surfaces. The TGA curves demonstrate an intense weight loss for the Hartley granite (0.461 wt%) in the temperature range from 688 K to 899 K and for the Quarry granite (0.222 wt%) from 723 K to 876 K. The DTG curve of Hartley granite in this temperature range contains a peak at 873 K and a broad shoulder from 688 K to 826 K, where the former indicates the dehydration of mica while the latter could indicate the dehydration of fluid inclusion due to alteration (Guggenheim et al., 1987; Johnson and Rossman, 2004). The DTG curve of Quarry granite show one peak at 844 K, indicating the dehydration of mica (Guggenheim et al., 1987). The water content in the Quarry granite continued decreasing after 876 K, probably associated with dehydration of amphibole (Földvári, 2011).

Table 2
The modal composition of the granite samples determined by point counting and the water content of the major minerals determined by FTIR.

Minerals	Modal composition (wt%)		Water content (ppm)	
	HGND/HGNP	QGND/QGNP	HGND/HGNP	QGND/QGNP
Quartz	41.5	36.2	–	56(±37)
Plagioclase	33.1 ($An_{12}Ab_{87}Or_1$)	47.9 ($An_{18}Ab_{81}Or_1$)	–	1348 (±211)
K-feldspar	24.7 (Ab_8Or_{92})	11.0 ($Ab_{13}Or_{87}$)	–	716 (±320)
Accessory minerals	0.6	4.4		

Fig. 4 shows the infrared absorption spectra for quartz, plagioclase, and K-feldspar in the Quarry granite before the conductivity measurements were performed. The absorption bands between 3000 cm^{-1} and 3800 cm^{-1} are due to the hydroxyl. Quartz shows multiple absorption bands in which the 3378 cm^{-1} band indicates hydrogen bonding to Al^{3+} (forming Al-H triplet), and the broad band from 3000 cm^{-1} to 3700 cm^{-1} indicates hydrogen as molecular or molecular clusters in inclusions (Potrafke et al., 2019). Feldspars also incorporate several species of hydrogen that are structurally bonded in the lattice (Johnson, 2006). The term "water" refers to all the hydrous species in the 3000 cm^{-1} to 3800 cm^{-1} range and the water content of the minerals was calculated using the modified Beer-Lambert law (Rossman, 2006). For quartz, the integral molar absorption coefficient derived from the calibration graph was 89,000 ± 15,000 L/mol.H_2O.cm^{-1} (Thomas et al., 2009). The absorption coefficients used for K-feldspar and plagioclase were 120,470 ± 11,360 L/mol. H_2O. cm^{-1} and 202,600 ± 20,260 L/mol. H_2O. cm^{-1}, respectively (Mosenfelder et al., 2015). The quartz was found almost anhydrous (56 ± 37 ppm.H_2O). The water content in plagioclases was considerably higher than in the K-feldspars.

3.2. Electrical conductivity

Representative impedance spectra are presented in Fig. 5. The arcs in the spectra are due to conduction in the grain interiors, while the tails are probably due to the polarization of ions between the electrode surface and the sample (Yoshino, 2010). The impedance spectra were fitted with the equivalent circuits consisting of a resistor and a constant phase element in parallel, and subsequently the resistance of the resistor was then used to calculate the electrical conductivity (σ) using the equation:

$$\sigma = l/(SR) \quad (1)$$

where S is the surface area of the sample (m^2), l is the thickness of the sample (m), and R is the electrical resistance (Ohm). The Arrhenius equation:

Table 1
The chemical composition of the two natural granite samples analyzed by X-ray fluorescence spectroscopy and EMPA.

	Hartley Granite				Quarry Granite					
	XRF for whole rock	Plagio	K-feld	Qtz	XRF for whole rock	Plagio	K-feld	Qtz	Mica	Amph
SiO2	75.54	64.57	65.12	99.42	74.464	64.38	62.63	99.45	45.01	54.49
TiO2	0.10	0.00	0.00	0.02	0.111	0	0.03	0	0.73	0
Al2O3	12.74	21.20	18.36	0.02	14.915	22.46	18.81	0.02	32.42	15.74
FeO	0.71	0.04	0.03	0.02	1.108	0.02	0.02	0	4.25	13.58
MnO	0.03	0.01	0.00	0.01	0.035	0	0	0.01	0.02	0.13
MgO	0.14	0.00	0.00	0.00	0.42	0	0	0.01	0.87	0.01
CaO	0.58	2.26	0.00	0.01	1.961	3.77	0.02	0	0	0.19
Na2O	3.77	4.77	0.94	0.01	4.755	9.38	1.35	0	0.26	8.28
K2O	5.03	0.27	15.50	0.01	1.867	0.14	14.17	0	10.57	0.04
NiO	0	0.02	0	0	0	0.01	0.02	0.02	0	0
P2O5	0.02	0.01	0.00	0.00	0.062	0.06	0.1	0.02	0	0
Total	98.64	93.54	99.96	99.51	99.698	100.2	97.13	99.53	94.13	92.46

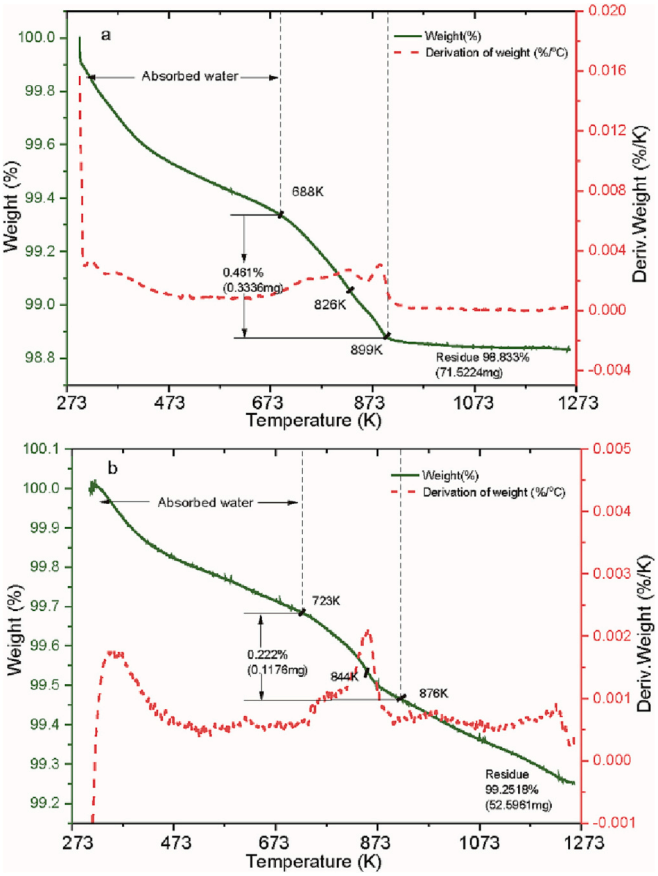

Fig. 3. Representative thermogravimetric analysis curves of the Hartley granite (a) and the Quarry granite (b) measured at a rate of 10 K/min. The green solid line represents the thermogravimetric analysis (TGA) curve; the red dash line represents the differential thermogravimetric curve (DTG). (For interpretation of the references to colour in this figure legend, the reader is referred to the web version of this article.)

$$\sigma = A\, exp\{-\Delta H/(kT)\} \quad (2)$$

where T is the absolute temperature in Kelvin (K), A is a pre-exponential factor (S/m), ΔH is the activation enthalpy (eV), and k is the Boltzmann constant (eV/K), was used to model the effect of temperature on the electrical conductivity. The parameter of A and ΔH were determined by fitting the experimental data to Eq. (2) (Table 3).

The electrical conductivities of all the samples were plotted as a function of the reciprocal temperature to fit the Arrhenius equation, and those for QGND and QGNP at 1 GPa were presented in Fig. 6. For both samples, the conductivity at the first heating stage (Heating 1) is higher than their first cooling stages (Cooling 1), probably due to the escape of moisture adsorbed in the assembly during the sample preparation (Yoshino, 2010). For the QGND sample, the electrical conductivity was measured in the first two cycles (from the Heating 1 to Cooling 2) below 873 K. Compared to this low temperature range, the conductivity increased by a half order of magnitude once the temperature increased to 1173 K during the third heating stage. The recovered sample show partial melts at grain boundaries. For the QGNP at 1 GPa, the conductivity was consistent at the second cycle, whereas it decreased by about a half order of magnitude relative to the second cycle once the temperature increased to 1273 K. This change may be associated with the escape of absorbed water in the assembly at high temperature, as this has also been reported for a powdered granulite (Fuji-ta et al., 2004). The electrical conductivity of the QGND was about one order of magnitude higher than that of the QGNP. No pervasive melt was observed in the QGNP after the conductivity measurement; however, isolated voids were found within a couple of feldspar grains probably indicating the early state of melting (Fig. S2). The activation enthalpy for QGND is determined from the cycles before melting, which means the conductivity values at the stages from the Cooling 1 to Heating 3. For QGNP, the activation enthalpy is determined by the Heating 3 to Cooling 3 after the escape of absorbed water.

The electrical conductivities for all the samples are compiled in Fig. 7. At ambient pressure, the two granites show comparable conductivities at all temperature ranges. However, the conductivities of the powdered granite samples were about 1.5 orders of magnitude higher than their drilled counterparts. Analogous to conductivity, the activation enthalpies of the HGNP (0.76 eV) and QGNP (0.88 eV) samples are

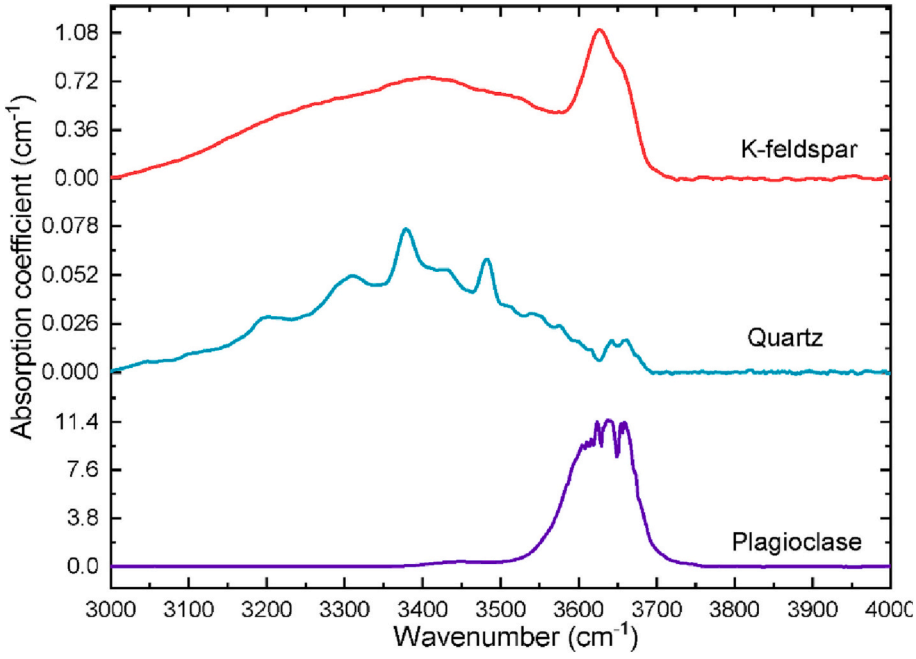

Fig. 4. Representative FTIR spectra of the constitutive minerals in Quarry Granite.

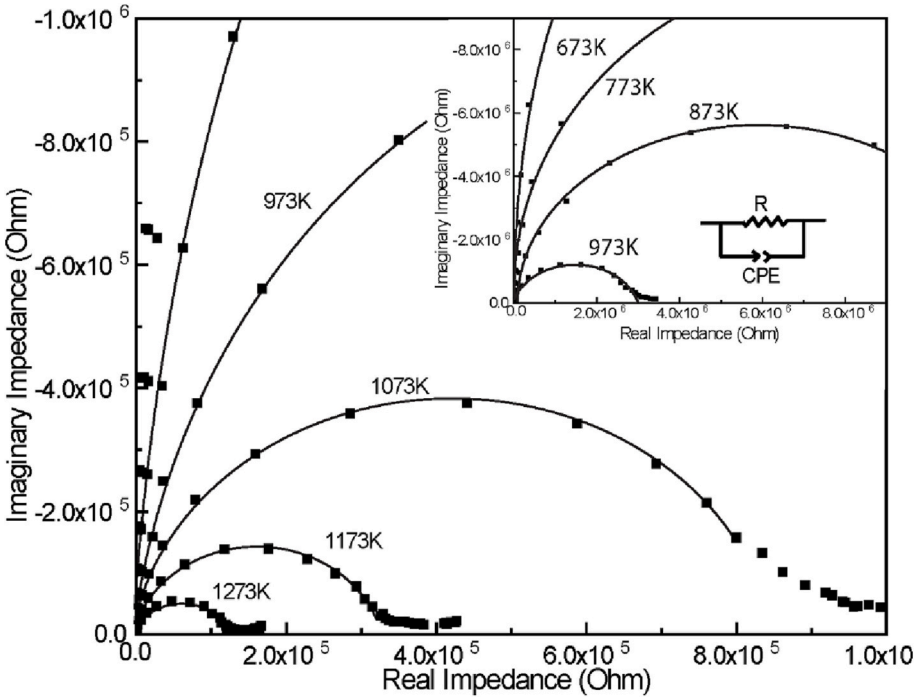

Fig. 5. Representative complex impedance spectra from the QGNP sample at 1 GPa and 673 to 1273 K. The solid squares mark the measured impedance, and the solid lines are the lines of best fit using an equivalent circuit of R-CPE in parallel. The tails of each impedance arc were ignored in the fitting. The insert shows the spectra at the temperature from 673 to 973 K.

Table 3
The temperature and pressure conditions for all measurements together with the parameters fitted to Arrhenius equation and water contents.

Samples	Temperature (K)	Pressure	ΔH(eV)	$\log_{10}A$ (S/m)	Sample description
Qtz-R	673–1173	Am	1.06 (±0.02)	1.63	Core drilled natural quartz [C_w = 940 (± 285)[1]]
Ab-R	673–1173	Am	1.24 (±0.05)	4.85	Core drilled natural albite [C_w = 11 (5)[1]]
Or-R	673–1173	Am	1.41 (±0.05)	4.18	Core drilled natural albite [C_w = 468 (± 133)[1]]
HGND	673–773	Am	1.220 (±0.063)	9.906	Core drilled Hartley granite
HGNP	573–873	Am	0.760 (±0.007)	3.165	Powdered Hartley granite
QGND	673–773	Am	1.210 (±0.059)	14.335	Core drilled Quarry granite
QGNP	573–873	Am	0.880 (±0.009)	1.697	Powdered Quarry granite
QGND	573–873	1GPa	0.837 (±0.033)	417.446	Core drilled Quarry granite
	873–1173		0.773 (±0.012)	759.451	
QGNP	573–823	1GPa	0.824 (±0.035)	4.935	Powdered Quarry granite
	873–1273		1.085 (±0.068)	210.087	
HGSP	773–1273	1 GPa	1.01	23.55	Synthetic Hartley granite powder
QGSP	773–1273	1 GPa	1.19	346.178	Synthetic Quarry granite powder

similar, whereas they are remarkably lower than the HGND (1.22 eV) and QGND (1.21 eV). The difference in conductivity and activation energy between the powdered and core drilled samples could be due to the mechanical pulverization that produces numerous defects at the grain boundaries. At 1 GPa, the QGSP showed higher conductivity than the HGSP, in line with the conductivity dependence on the abundance of feldspars. Compared to the QGNP, the QGSP had lower conductivities. The conductivities of the QGNP at 1 GPa were >0.5 orders of magnitude higher than that at ambient pressure. This is probably due to that the high porosities of the samples at ambient pressure reduce the conductivity. The Ab-R shows a similar conductivity to the Or-R, lower than that of the Qtz-R. The three single phases are about one order of magnitude lower in conductivity than that for the mixed sample (HGSP and QGSP) at 1 GPa.

4. Discussion

4.1. Comparisons with previous studies

The electrical conductivity of the major minerals and granite in this study were compared on an individual basis with those of previous studies. As shown in Fig. 8, the Or-R and Ab-R have remarkably lower electrical conductivities than their counterparts in powdered form (Or-P and Ab-P) as reported in our previous study (Han et al., 2021) and other studies (Wang et al., 2014a; Hu et al., 2013, 2014; Guo et al., 2015; Yang et al., 2012). The conductivity of Or-R and Ab-R could have bias against an orientation to some extent due to the anisotropic structure, although the differences in conductivity among the distinct orientations are less than one order of magnitude (Wang et al., 2014b; Yang et al., 2012). Qtz-R shows slightly lower conductivity than its powder counterpart (Qtz-P) (Han et al., 2021), comparable to polycrystalline quartz (Bagdassarov and Delépine, 2004). The differences in the conductivities of quartz among the distinct orientations can be as large as two orders of magnitude, much larger than those for anisotropic albite and orthoclase (Wang et al., 2014a; Yang et al., 2012; Wang et al., 2010). In this study, focus has been given to the relationship between the conductivity of

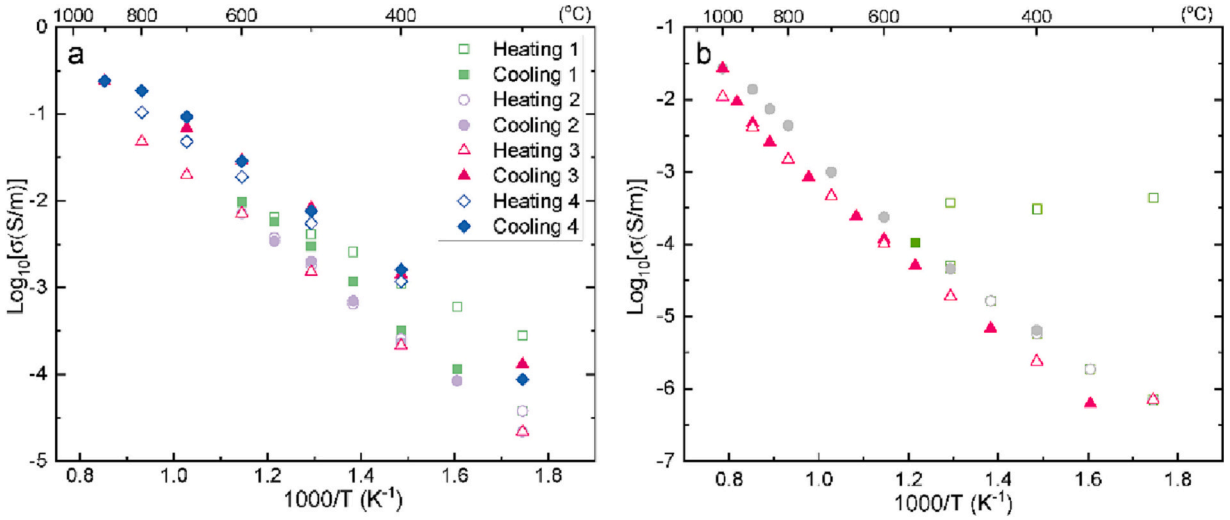

Fig. 6. The electrical conductivity of (a) the QGND sample and (b) the QGNP sample at 1 GPa.

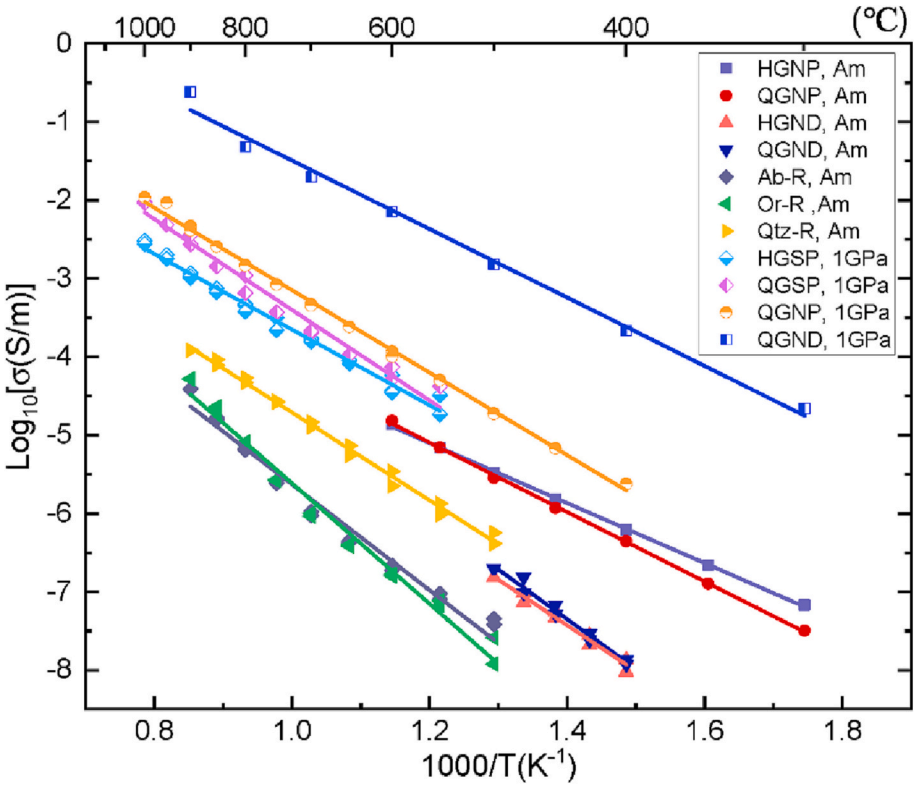

Fig. 7. The electrical conductivity vs the reciprocal temperature for the core drilled and the powdered granite samples measured at both ambient pressure (Am) and 1 GPa. The solid lines are the lines of best fit.

granite and the constitutive minerals instead of seeking to discuss comprehensively the cause for the differences in the conductivity for each mineral by referring to studies on the individual minerals.

The electrical conductivities of all the granite samples were measured under dry conditions in this study. Given that the conductivity of QGND at 1 GPa was abnormally high, it is projected that the conductivity was dominated by accessory minerals with a large grain size (about 1 mm) relative to the Al_2O_3 capsule (Φ2 mm × 1.5 mm) and thus these data were excluded in Fig. 8d (Saltas et al., 2020). The weakly preferred orientation in both granites indicates a negligible influence of the fabric on electrical conductivity (Fig. 2). Pressure effect on the conductivity of granite can also be neglected as indicated from the conductivity measurements of the biotite granite at different pressures (Dai et al., 2014). The conductivities of HGND and QGND are comparable to the monzonitic granite from Wutai Mountain in Shanxi Provence, China (SXW), which comprises 58% feldspar and 37% quartz (Dai et al., 2014). However, the HGND and QGND are lower in electrical conductivity compared to the values for most granites reported (Dai et al., 2014; Shanov et al., 2000; Olhoeft, 1981; Guo et al., 2017), likely a reflection of the compositional differences of the constitutive minerals. For example, the HGND and QGND have lower conductivities than the XHS8 granite with 62% feldspar and 35% quartz, probably due to the lower abundance of feldspars and accessory minerals that are supposed to control the conductivity of granite (Olhoeft, 1981). The QGNP

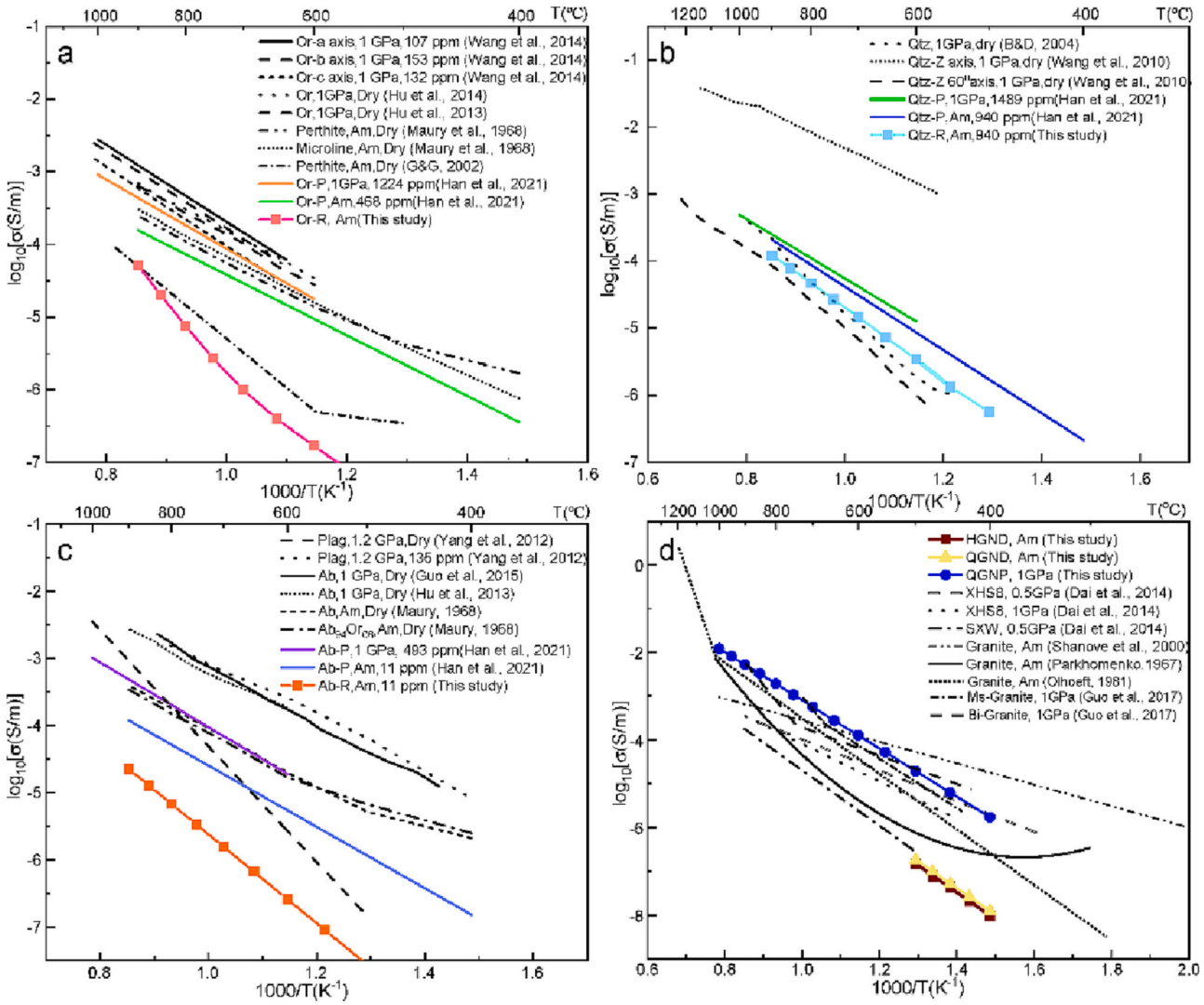

Fig. 8. The electrical conductivity of granite and constitutive quartz, orthoclase and albite in this and previous studies. Ms-Muscovite, Bi-Biotite.

measured at 1 GPa shows comparable electrical conductivity to the data for granite in previous studies (Shanov et al., 2000; Olhoeft, 1981; Dai et al., 2014; Guo et al., 2017).

4.2. *Hydrous accessory minerals*

The hydrous accessory minerals, including muscovite, biotite, and amphibole, exert negligible effects on the electrical conductivity before their dehydration or breakdown, due to their low abundances in granite. Olhoeft (1981) found negative dependence of granite conductivity on quartz abundance and thus implied that the conductivity of granite is controlled by total abundance of accessory minerals and feldspars. In Fig. 9, the effect of the abundance of accessory minerals on the conductivity of granite at 823 K is illustrated. The distinct abundance of accessory minerals in HGND (0.6 vol%) and QGND (4.4 vol%) shows comparable conductivities. This finding agrees well with previous study of Dai et al. (2014), in which the conductivity is independent on the abundance of the accessory minerals (<5%). Nevertheless, experimental observations suggest that a threshold of 16 vol% is required to allow the conductive phase distributed randomly to control the conductivity of a mixture, which was supported by the percolation theory (Han and Clark, 2021; Sun et al., 2021). Since accessory minerals in our sample only account for a few percent of the total weight percentage in granite, we conclude that the accessory minerals have a mostly negligible effect on

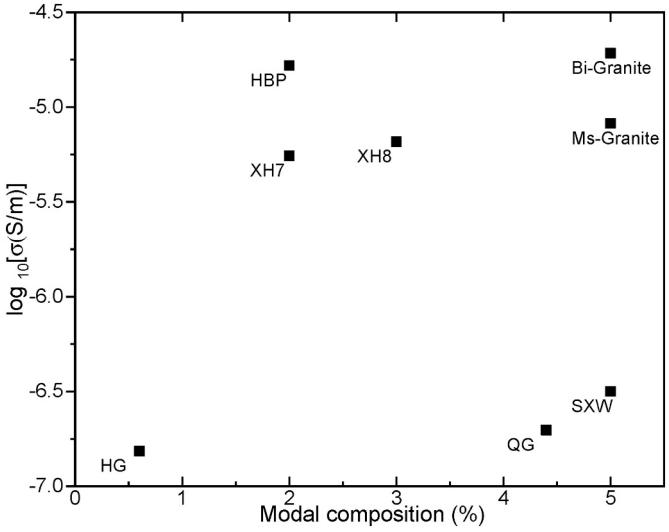

Fig. 9. The electrical conductivity vs modal composition of accessory minerals in granite at 823 K. The HBP, XH7, SXW, and XH8 were derived from Dai et al. (2014). The Bi-Granite and Ms-Granite were derived from Guo et al. (2017).

the conductivity of granite at temperatures within the stability of hydrous accessory minerals in our samples.

The influence of hydrous accessory minerals on the conductivity of granite is primarily linked to their dehydration at a high temperature. Muscovite is generally the first mineral to be dehydrated, followed by biotite, and amphibole as temperature increases. Muscovite dehydrates approximately from 688 K at ambient pressure (Fig. 3), but the conductivity of the HGND and QGND did not change significantly till 773 K. Similarly, the dehydration temperature of muscovite is about 975–1000 K at 1 GPa (Gardien et al., 2000) and the dehydration did not affected the conductivity of QGNP till 1273 K at 1 GPa. Dehydration of muscovite releases aqueous fluid that directly reacts with quartz and feldspar in granite and generate melt (via: Quartz + Alkali feldspars + Muscovite + H_2O = Melt), namely, dehydration melting (Johannes and Holtz, 2012). Approximately 18 vol% of muscovite is required to produce a percentage of melt of 8– 9 vol% that forms an interconnected mobile melt at grain boundaries in an undeformed granite (Dyck et al., 2020). Biotite starts to dehydrate at about 1123 K at 1 GPa, despite varying with the concentration of Ti^{3+}, F^{-}, and Cl^{-} (Gardien et al., 2000; Finch and Tomkins, 2017). The temperature for dehydration melting of amphibole is generally higher than that for biotite and also varies considerably with the elements (Wolf and Wyllie, 1994). Given the absence of pervasive melts but alveolate voids in QGNP (Fig. S2) and the effect of time on the melting of hydrous minerals, we propose that a low fraction of hydrous minerals failed to form an interconnected system of melt during the short time of conductivity measurements. We suggest that this also accounted for the consistent conductivity of granite over 1273 K in previous studies as shown in Fig. 8, but unfortunately their samples were not imaged after measurements (Dai et al., 2014; Olhoeft, 1981). Given that oxygen is also produced along with water during the dehydration of mica and amphibole, the oxidization of Fe^{2+} to Fe^{3+} induces small polaron conduction that increases the electrical conductivity by orders of magnitude (Hu et al., 2018; Saltas et al., 2020). Nevertheless, the enhanced conductivity of oxidized minerals could hardly affect the conductivity of granite because their modal composition is usually less than the threshold for percolation (16%).

The fabric of oriented and prolonged hydrous minerals could affect the bulk conductivity of granite by facilitating the connectivity of the dehydration melts. Guo et al. (2017) reported an abrupt increase in the conductivity of a deformed muscovite (5 vol%)-granite and a biotite (3 vol%)-granite at 930 K and 1000 K, respectively, indicating the dehydration melting of muscovite and biotite (Fig. 8). By contrast, the consistence of conductivities at temperatures above 1000 K were observed in the undeformed Hartley and Quarry granites and other granites in previous studies (Fig. 8). Strong shear deformation distorts and prolongs the soft minerals, especially mica, enhancing the connectivity of mica and changing of the dihedral angles; thus the dehydration melts could form an interconnected network once the dehydration melting point of mica is reached (Kawano et al., 2012; Yin et al., 2017). Additionally, deformation induces a change in the distribution of the fluid/melt from the isolated pores to the wetted grain boundaries (Tullis et al., 1996), which form an interconnected network of grain boundaries and this increases the conductivity of a rock. Therefore, the dehydration melting of mica could increase the conductivity of a deformed granite at a relatively low temperature (about 970 K at 1 GPa) despite a low abundance of mica. Thus, we conclude that the dehydration melting of undeformed granite with low concentration of hydrous minerals cannot promote the bulk conductivity significantly until an interconnected melt system is formed.

4.3. Conduction mechanism and the effect of water on the conductivity of granite

The conductivity of a multiphase assemblage is controlled by the conductivities of the constitutive mineral, which may have a variety of conductivity mechanisms. The conduction mechanism for quartz is related to the hopping of either H^{+} or alkali ions that are bound to Al^{3+} forming an Al-M triplet (Amulele et al., 2019; Wang et al., 2010). For dry feldspars, including plagioclase and K-feldspars, the charge carriers are thought to be alkali ions (Na^{+} or K^{+}).However, water incorporation in feldspar will generate more vacancies, which provides more passes for the migration of alkali ions and therefore enhances the bulk conductivity. It has been well documented that the electrical conductivity of feldspars increases with the content of structural water (Yang et al., 2012; Amulele et al., 2022; Yang, 2012; Hu et al., 2022). The higher electrical conductivity of QGNP than that of QGSP at 1 GPa (Fig. 7) well supported it, where the water content of feldspars (1348 ppm in plagioclase +716 ppm in orthoclase) in QGNP is higher than those in QGSP (11 ppm in albite +468 ppm in orthoclase). Dai et al. (2014) modeled quantitatively the conductivity of granite by applying X_A [X_A = $(Na_2O + K_2O + CaO)/SiO_2$] of the bulk composition to represent the dependence of conductivity on the chemical composition at 1 GPa, where the conductivity increases with X_A. We used Dai's model (Dai et al., 2014) to calculate the conductivity of the Quarry granite (X_A = 0.12) and it was found to be inconsistent with the SXW (X_A = 0.12) and other granites with similar X_A (Fig. 10). This modeled conductivity is also about 1.5 orders of magnitude lower than the measured conductivity of QGNP at 1 GPa. The aforementioned model was developed based on using dry granites without structural water in the constitutive minerals; the water effect thus has been neglected when modeling the conductivity of granite (Dai et al., 2014). Therefore, the water content of feldspars should be incorporated into the modeling of the electrical conductivity of granite.

4.4. Geological implications

We apply granitoids to present a broad range of quartz-feldspar proportions (Winter, 2013). The electrical conductivity of a granitoid is determined by the conductivities of major minerals and their spatial alignments. The former is linked to the chemical composition and water content of major minerals, while the latter depends on the proportion and anisotropy of the constituents, as well as the fabric of the granitoid. The alignment of anisotropic minerals could result in orientational preferences of electrical conductivity in a deformed granitoid (Wang et al., 2010; Kluge et al., 2022). Given the anisotropic conductivity of feldspars and quartz, the conductivity data of polycrystal minerals were used rather than single crystals to model the conductivity of an undeformed granitoid (Wang et al., 2010; Yang, 2012). Given that the conductivity of dry feldspars is dependent on the ratio of Na/K, the conductivity parameters derived from the polycrystalline plagioclase ($An_{66}Ab_{32}Or_2$) (Yang et al., 2012), orthoclase Or-P ($Or_{67}Ab_{33}$) (Han et al., 2021), and Qtz-P (Qtz_{100}) (Han et al., 2021) were adopted to represent the plagioclase, K-feldspar and quartz in a granitoid, respectively.

The effect of water (hydrogen) on the electrical conductivity differs for quartz, K-feldspar, and plagioclase. The water species that is bound to Al^{3+} in the Al-H triplet is likely to be responsible for the electrical conductivity of quartz. The amount of this water is typically <40 ppm (Johnson, 2006), contrasted with the water of molecular cluster or fluid inclusion in Qtz-R, as inferred in (Han et al., 2021). Additionally, Na^{+} could be a superior contributor to the electrical conductivity of quartz compared to the hydrogen in Al-H triplet (Amulele et al., 2019). Therefore, it is believed that the water content is insignificant to the electrical conductivity of quartz, and this is supported by a similar conductivity for quartz with distinct water contents (Fig. 8b). The electrical conductivity of plagioclase and K-feldspar exhibits a positive dependence on the water content (Yang et al., 2012; Amulele et al., 2022; Hu et al., 2022). Although water in plagioclase and K-feldspar could exist in several species with varying content, structural OH^{-} is likely to be the primary species contributing to the electrical conductivity of the hydrous feldspars, and the content of these waters is reported to be <915 ppm (Johnson, 2006; Amulele et al., 2022). As it is

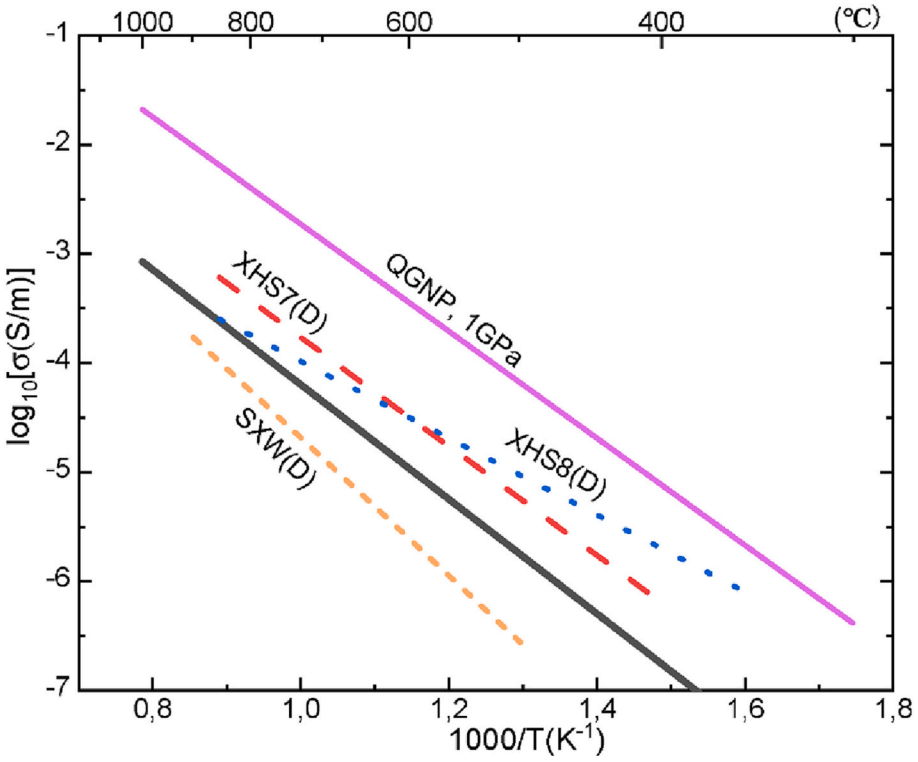

Fig. 10. Comparison of the measured conductivity of QGNP to the modeled conductivity of the Quarry granite at 1 GPa. The black solid line represents the modeled conductivity of the Quarry granite using X_A (0.12) suggested by Dai et al. (2014). The X_A of the XHS7(D), XHS8(D). and SXW(D) is 0.14, 0.13, and 0.12, respectively (Dai et al., 2014).

not yet determined how water partitions between quartz and feldspar in granitoids, in the present study it is assumed that the plagioclase and K-feldspar are both able to incorporate a maximal concentration of water (915 ppm). The highest conductivities of plagioclase and K-feldspar in a granitoid were calculated using the relationship between the water content and the conductivity as proposed by Yang et al. (2012):

$$\sigma = A \cdot C_w^{0.83} exp(-\Delta H/kT) \quad (3)$$

where C_w is the water content (wt%). The pre-exponential term (A), the activation energies (ΔH) of plagioclase ($An_{66}Ab_{32}Or_2$) and K-feldspar ($Or_{67}Ab_{33}$) were adopted from Yang et al. (2012) and Han et al. (2021), respectively. Here, we use the Hashin–Shtrikman (HS) model to provide the upper and the lower bounds for the conductivity of a granitoid (Hashin and Shtrikman, 1961):

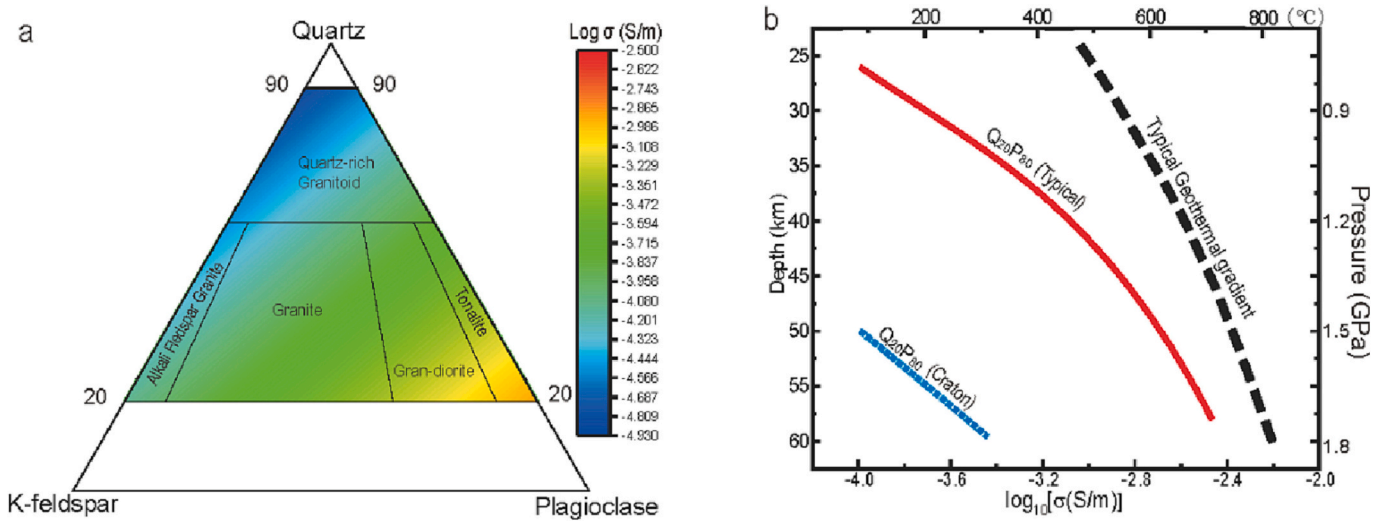

Fig. 11. The electrical conductivity of a granitoid at 700 °C combined by varying the modal compositions of quartz, K-feldspar, and plagioclase with the highest water content (915 ppm. H_2O) (a) and the maximal electrical conductivity vs depth (b). The upper bound of Hashin–Shtrikman model is used to model the highest conductivity of each composition in (a). The temperature as a function of depth (dashed black line) represents a typical geothermal gradient for a continent adopted from Winter (2013). The red solid line represents the conductivity calculated based on a typical geothermal gradient of the continental crust, while the blue dotted line is calculated based on the geothermal gradient of an old craton (Rudnick and Nyblade, 1999). (For interpretation of the references to colour in this figure legend, the reader is referred to the web version of this article.)

$$\sum(s) = \left(\sum_{i=1}^{N} \frac{f_i}{\sigma_i + 2s} \right)^{-1} - 2s \quad (4)$$

where s is either the maximal or minimal conductivity for the plagioclase, K-feldspar, and quartz. The σ_i and f_i are the conductivity and the volume fraction of the ith components, respectively. Tonalites consisting of 20 vol% quartz and 80 vol% plagioclase ($Q_{20}P_{80}$) show the highest electrical conductivity (Fig. 11a). The conductivity of quartzite and syenite in the calculation was excluded because these granitoid types occur only in specific geological settings, such as hot spot and/or continental rifting (Winter, 2013). The tonalite with a composition of $Q_{20}P_{80}$ was used to calculate the maximal electrical conductivity of a granitoid at a depth from 25 to 60 km, shown in Fig. 11b, subject to the geotherms in different geological settings. The maximal conductivity can be as high as about 0.004 ± 0.0001 S/m (250 Ω·m) at 60 km under orogenic regions where the typical geothermal gradient applies. The maximal conductivity provides the upper limit for the conductivity of the most undeformed granitoids without partial melt or aqueous liquid. The lower geothermal gradient under a stable continental craton leads to a significantly lower conductivity, although the geotherms of cratons are dependent on the ages and the concentration of radioactive elements (Artemieva, 2006). A geothermal gradient of 10 °C/km was used to calculate the conductivity under an old stable craton (Fig. 11b) (Rudnick and Nyblade, 1999). The dehydration melting of a granitoid is not likely to occur in an old cratonic setting, as the crustal thickness of a craton is normally 40 ± 5 km corresponding to 400 ± 50 °C, a temperature much less than the dehydration temperature of muscovite (~700 °C/973 K) at 1.2 GPa (Rudnick and Nyblade, 1999).

The maximal conductivity of a granitoid is compared with the magnetotelluric (MT) observations from different geological settings to constrain the interpretation of crustal structures (Fig. 12). The felsic gneisses under the Mesoarchaean-Palaeoproterozoic North Gawler Craton, South Australia, shows conductivities (Selway et al., 2011) well below the maximal conductivity. The old subduction-related St. Peter Suite in South Australia has conductivity lower than the maximal conductivity although higher than those under the cratonic crust (Thiel and Heinson, 2010). Although the chemical composition of a granitoid may be altered by old arc magmatisms and recycling of crustal sediments to introduce water or form conductive phases (Swain et al., 2008), they are not necessarily required to explain the conductivity characteristics. The Curnamona Province show higher conductivity (Robertson et al., 2016) than the maximum in the crustal regime, indicating alternative causes rather than the structural water in a granitoid. The absence of an abrupt increase in conductivity also refutes the possibility of dehydration melting in the middle-to-lower crust of the Curnamona Province. The geothermal gradient under the Curnamona Province is abnormally high (~92 mW/m2), probably due to the prolonged high thermal gradient metamorphism e between 1600 and 1580 Ma and the radiogenic granite thickened the crust (Van Leeuwen et al., 2022; Neumann et al., 2000). We calculated the electrical conductivity profile under the Curnamona Province based on the composition in Fig. 11, and the resultant conductivity is lower than the MT observation above 40 km. This implies that the high conductivity could be linked to the formation of fertile veins or the abundance of accessory minerals during the metamorphism (Van Leeuwen et al., 2022; Özaydın et al., 2022). The conductivity under the orogenic Lhasa Terrane in Tibet (Wang et al., 2014a) starts to increase below the middle crust (>20 km) and surpasses the maximal conductivity of a granitoid below 45 km. This increase in conductivity is likely attributed to a high geotherm (850–1000 °C at a depth of 50 km) under the Lhasa Terrane, which allows the dehydration melting of biotite and amphibole to form an interconnected melt system in the granitoids, consistent with the low velocity imaged from the seismology and volcanic activities (Wang et al., 2016; Nelson et al., 1996). Alternatively, the upwelling of melts or volatiles could also induce the conductive anomaly under the Tibet (Liang et al., 2018). Therefore, the conductivity higher than the maximal conductivity under granitic crust hardly resulted from the hydrous accessory minerals and water in minerals, indicating other geological process such as fertilization, partial melting due to biotite and amphibole, and infiltration of aqueous fluid.

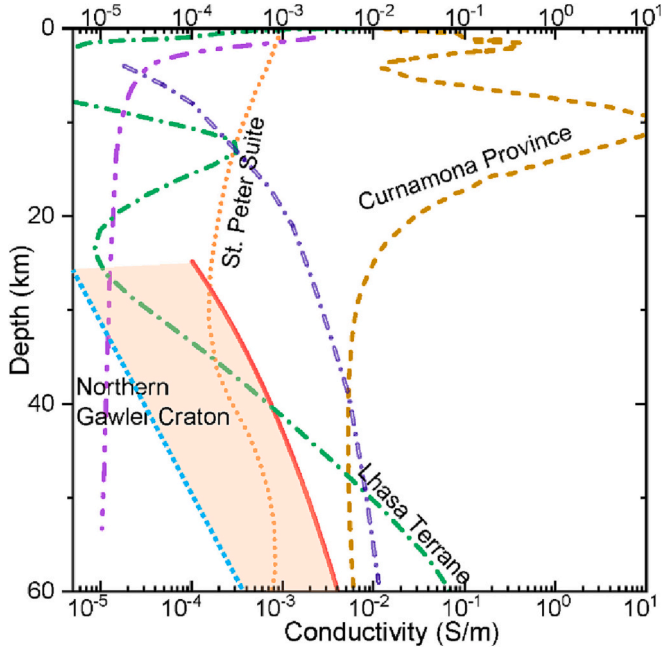

Fig. 12. Conductivity-depth profile through the St. Peter Suite on the Gawler Craton in South Australia (Thiel and Heinson, 2010), the Northern Gawler Craton (Selway et al., 2011), the Curnamona Province in South Australia (Robertson et al., 2016), and the Lhasa Terrane in Tibet (Wang et al., 2014). The red solid line and blue dash line are the maximal conductivity of a granitoid under a typical and craton geotherm, respectively (based on Fig. 11b). The hole purple dash-dot line is the calculated electrical conductivity profile under the Curnamona Province. (For interpretation of the references to colour in this figure legend, the reader is referred to the web version of this article.)

5. Concluding remarks

The electrical conductivity of two undeformed granites from Hartley, NSW, Australia and Rocklin, California, USA was studied at various temperatures and pressures. Hydrous accessory minerals were found to barely affect the conductivity of granite until an interconnected melt system at grain boundaries is formed. The structural water content in the feldspars could significantly affect the electrical conductivity of the granite. The maximal conductivity of granitic rocks (granitoids), combined with the effect of water on the minerals and the modal composition, provides the upper limit of granitoid conductivity for the interpretation of crustal structures from MT observations. This upper limit was applicable to different geological settings, including a cold craton of the North Gawler Craton, an old subduction arc of the St. Peter Suit, the tectonically reworked Curnamona Province and an active orogen of the Lhasa Terrane. This maximal conductivity of a granitoid could also be applied to alternative crustal regions; however, careful examination of the lithology and the representativity is required.

CRediT authorship contribution statement

Kui Han: Conceptualization, Writing – original draft, Investigation. **Xinzhuan Guo:** Writing – review & editing. **Xuben Wang:** Resources. **Junfeng Zhang:** Resources. **Sinan Özaydin:** Writing – review & editing. **Dewei Li:** Data curation. **Simon Martin Clark:** Funding acquisition, Visualization, Project administration.

Declaration of Competing Interest

The authors declare that they have no known competing financial interests or personal relationships that could have appeared to influence the work reported in this paper.

Data availability

Data will be made available on request.

Acknowledgement

We would like to thank, Jiayuan Bai, Dr. Xiong Wang and Dr. Qingbo Xia for the help in conducting experiments, as well as the input from Dr. Richard Flood. This work was support by Australian Research Council Discovery Project (DP160103502), Natural Science Foundation of China (42230311) and Open Research Program (GPMR201801) funded by State Key Laboratory of Geological Processes and Mineral Resources, China University of Geosciences, Wuhan. Kui Han would like to thank Macquarie University for an International Research Training Scholarship (iRTP) and Chengdu University of Technology for starting-up grant (10912-KYQD2020-08600). This work is indebted to the Centre of Excellence for Core to Crust Fluid System, Australia for facilitating the research work.

Appendix A. Supplementary data

Supplementary data to this article can be found online at https://doi.org/10.1016/j.tecto.2023.229857.

References

Amulele, G.M., Lanati, A.W., Clark, S.M., 2019. Electrical conductivity studies on silica phases and the effects of phase transformation. Am. Mineral. 104, 1800–1805. https://doi.org/10.2138/am-2019-7120.

Amulele, G.M., Lanati, A.W., Clark, S.M., 2022. The electrical conductivity of albite feldspar: Implications for oceanic lower crustal sequences and subduction zones. American Mineralogist. J. Earth Planet. Mat. 107 (4), 614–624.

Aranovich, L.Y., Makhluf, A.R., Manning, C.E., Newton, R.C., 2014. Dehydration melting and the relationship between granites and granulites. Precamb. Res 253, 26–37.

Artemieva, I.M., 2006. Global 1× 1 thermal model TC1 for the continental lithosphere: implications for lithosphere secular evolution. Tectonophysics 416 (1–4), 245–277.

Bagdassarov, N.S., Delépine, N., 2004. α–β inversion in quartz from low frequency electrical impedance spectroscopy. J. Phys. Chem. Solids 65, 1517–1526.

Bish, D.L., Duffy, C.J., 1990. Thermogravimetric analysis of minerals. In: Stucki, J.W., Bish, D.L., Mumpton, F.A. (Eds.), Thermal Analysis in Clay Science. Clay Minerals Society, Boulder, Colorado, pp. 95–157. https://doi.org/10.1346/CMS-WLS-3.4.

Chen, S., Guo, X., Yoshino, T., Jin, Z., Li, P., 2018. Dehydration of phengite inferred by electrical conductivity measurements: Implication for the high conductivity anomalies relevant to the subduction zones. Geology 46, 11–14. https://doi.org/10.1130/G39716.1.

Dai, L., Hu, H., Li, H., Jiang, J., Hui, K., 2014. Influence of temperature, pressure, and chemical composition on the electrical conductivity of granite. Am. Mineral. 99, 1420–1428.

Duba, A., Heikamp, S., Meurer, W., Mover, G., Will, G., 1994. Evidence from borehole samples for the role of accessory minerals in lower-crustal conductivity. Nature 367 (6458), 59–61.

Dyck, B., Waters, D.J., St-Onge, M.R., Searle, M.P., 2020. Muscovite dehydration melting: Reaction mechanisms, microstructures, and implications for anatexis. J. Metamorph. Geol. 38, 29–52. https://doi.org/10.1111/JMG.12511.

Finch, E.G., Tomkins, A.G., 2017. Fluorine and chlorine behaviour during progressive dehydration melting: Consequences for granite geochemistry and metallogeny. J. Metamorph. Geol. 35, 739–757. https://doi.org/10.1111/jmg.12253.

Földvári, M., 2011. Handbook of thermogravimetric system of minerals and its use in geological practice. Budapest.

Fuji-ta, K., Katsura, T., Tainosho, Y., 2004. Electrical conductivity measurement of granulite under mid-to lower crustal pressure—temperature conditions. Geophys. J. Int. 157 (1), 79–86.

Gardien, V., Thompson, A.B., Ulmer, P., 2000. Melting of biotite+ plagioclase+ quartz gneisses: the role of H2O in the stability of amphibole. J. Petrol. 41 (5), 651–666.

Guggenheim, S., Chang, Y.H., Koster van Groos, A.F., 1987. Muscovite dihydroxylation: high-temperature studies. Am. Mineral. 72 (5–6), 537–550.

Guo, X., Yoshino, T., Shimojuku, A., 2015. Electrical conductivity of albite-(quartz)-water and albite-water-NaCl systems and its implication to the high conductivity anomalies in the continental crust. Earth Planet. Sci. Lett. 412, 1–9.

Guo, Y.X., Wang, D.J., Zhou, Y.S., Liu, Z.Y., Yu, Y.J., Li, D.Y., Zhang, D.N., Zhu, A.Y., 2017. Electrical conductivities of two granite samples in southern Tibet and their geophysical implications. Sci. China Earth Sci. 60 (8), 1522–1532. https://doi.org/10.1007/s11430-016-9046-7.

Guo, X., Zhang, L., Su, X., Mao, Z., Gao, X.-Y., Yang, X., Ni, H., 2018. Melting inside the Tibetan Crust? Constraint from Electrical Conductivity of Peraluminous Granitic Melt. Geophys. Res. Lett. 45, 3906–3913. https://doi.org/10.1029/2018GL077804.

Han, K., Clark, S.M., 2021. Review of calculating the electrical conductivity of mineral aggregates from constituent conductivities. Solid Earth Sci. 6 (2), 111–128.

Han, K., Guo, X., Zhang, J., Wang, X., Clark, S.M., 2021. Fast grain-boundary ionic conduction in multiphase aggregates as revealed by electrical conductivity measurements. Contrib. Mineral. Petrol. 176 (10), 1–19.

Hashin, Z., Shtrikman, S., 1961. Note on a variational approach to the theory of composite elastic materials. Journal of the Franklin Institute 271, 336–341.

Hu, H., Li, H., Dai, L., Shan, S., Zhu, C., 2013. Electrical conductivity of alkali feldspar solid solutions at high temperatures and high pressures. Phys. Chem. Miner. 40, 51–62.

Hu, H., Dai, L., Li, H., Jiang, J., Hui, K., 2014. Electrical conductivity of K-feldspar at high temperature and high pressure. Mineral. Petrol. 108, 609–618.

Hu, H., Dai, L., Li, H., Sun, W., Li, B., 2018. Effect of dehydrogenation on the electrical conductivity of Fe-bearing amphibole: Implications for high conductivity anomalies in subduction zones and continental crust. Earth Planet. Sci. Lett. 498, 27–37. https://doi.org/10.1016/j.epsl.2018.06.003.

Hu, H., Dai, L., Sun, W., Wang, M., Jing, C., 2022. Constraints on fluids in the continental crust from laboratory-based electrical conductivity measurements of plagioclase. Gondwana Res. 107, 1–12. https://doi.org/10.1016/j.gr.2022.02.011.

Johannes, W., Holtz, F., 2012. Petrogenesis and Experimental Petrology of Granitic Rocks. Springer Science & Business Media, pp. 100–112.

Johnson, E.A., 2006. Water in nominally anhydrous crustal minerals: speciation, concentration, and geologic significance. Rev. Mineral. Geochem. 62 (1), 117–154.

Johnson, E.A., Rossman, G.R., 2004. A survey of hydrous species and concentrations in igneous feldspars. Am. Mineral. 89 (4), 586–600.

Kawano, S., Yoshino, T., Katayama, I., 2012. Electrical conductivity of magnetite-bearing serpentinite during shear deformation. Geophys. Res. Lett. 39 (20), L20313.

Kluge, E.K., Toy, V., Lockner, D., 2022. Electrical Properties and Anisotropy of Schists and Fault Rocks from New Zealand's Southern Alps under Confining pressure. Geosciences 12 (3), 121.

Li, P., Guo, X., Chen, S., Wang, C., Yang, J., Zhou, X., 2018. Electrical conductivity of the plagioclase–NaCl–water system and its implication for the high conductivity anomalies in the mid-lower crust of Tibet Plateau. Contrib. Mineral. Petrol. 173 (16), 1–12. https://doi.org/10.1007/s00410-018-1442-9.

Liang, H., Jin, S., Wei, W., Gao, R., Ye, G., Zhang, L., Yin, Y., Lu, Z., 2018. Lithospheric electrical structure of the middle Lhasa terrane in the south Tibetan plateau. Tectonophysics 731, 95–103.

Litovchenko, A.S., Mazykin, V.V., 1984. Dehydroxylation effect upon electrical conduction of mica. Phys. Status Solidi A 81, 47–50.

Mosenfelder, J.L., Rossman, G.R., Johnson, E.A., 2015. Hydrous species in feldspars: a reassessment based on FTIR and SIMS. Am. Mineral. 100, 1209–1221.

Nédélec, A., Bouchez, J.L., 2015. Granites: Petrology, Structure, Geological Setting, and Metallogeny. OUP Oxford.

Nelson, K.D., Zhao, W., Brown, L.D., Kuo, J., Che, J., Liu, X., Klemperer, S.L., Makovsky, Y., Meissner, R.J.J.M., Mechie, J., Edwards, M., 1996. Partially molten middle crust beneath southern Tibet: synthesis of project INDEPTH results. Science 274 (5293), 1684–1688.

Neumann, N., Sandiford, M., Foden, J., 2000. Regional geochemistry and continental heat flow: implications for the origin of the south Australian heat flow anomaly. Earth Planet. Sci. Lett. 183 (1–2), 107–120.

Olhoeft, G.R., 1981. Electrical properties of granite with implications for the lower crust. J. Geophys. Res. Solid Earth 86, 931–936.

Özaydın, S., Selway, K., 2020. MATE: an analysis tool for the interpretation of magnetotelluric models of the mantle. Geochem. Geophys. Geosyst. 21, e2020GC009126 https://doi.org/10.1029/2020GC009126.

Özaydın, S., Selway, K., Griffin, W.L., Moorkamp, M., 2022. Probing the Southern African lithosphere with magnetotellurics: 2. linking electrical conductivity, composition, and tectonomagmatic evolution. J. Geophys. Res. Solid Earth 127, 1–28. https://doi.org/10.1029/2021jb023105.

Parkhomenko, E.I., 1982. Electrical resistivity of minerals and rocks at high temperature and pressure. Rev. Geophys. Space Phys. 20, 193–218 doi: 10.1029RG020i002p00193.

Potrafke, A., Stalder, R., Schmidt, B.C., Ludwig, T., 2019. OH defect contents in quartz in a granitic system at 1–5 kbar. Contrib. Mineral. Petrol. 174, 98. https://doi.org/10.1007/s00410-019-1632-0.

Robertson, K., Heinson, G., Thiel, S., 2016. Lithospheric reworking at the Proterozoic–Phanerozoic transition of Australia imaged using AusLAMP Magnetotelluric data. Earth Planet. Sci. Lett. 452, 27–35. https://doi.org/10.1016/j.epsl.2016.07.036.

Rossman, G.R., 2006. Analytical Methods for measuring Water in Nominally Anhydrous Minerals. Rev. Mineral. Geochem. 62, 1–28. https://doi.org/10.2138/rmg.2006.62.1.

Rudnick, R.L., Nyblade, A.A., 1999. The thickness and heat production of Archean lithosphere: constraints from xenolith thermobarometry and surface heat flow. Mantle petrology: field observations and high pressure experimentation: a tribute to Francis R.(Joe). Boyd 6 (6), 3–12.

Saltas, V., Pentari, D., Vallianatos, F., 2020. Complex electrical conductivity of biotite and muscovite micas at elevated temperatures: a comparative study. Materials (Basel) 13, 1–20. https://doi.org/10.3390/MA13163513.

Selway, K., 2014. On the causes of electrical conductivity anomalies in tectonically stable lithosphere. Surv. Geophys. 35, 219–257.
Selway, K.M., Hand, M., Payne, J.L., Heinson, G.S., Reid, A., 2011. Magnetotelluric constraints o the tectonic setting of Grenville-aged orogenesis in Central Australia. J. Geol. Soc. 168 (1), 251–264. https://doi.org/10.1144/0016-76492010-034.
Shanov, S., Yanev, Y., Lastovickova, M., 2000. Temperature dependence of the electrical conductivity of granite and quartz-monzonite from South Bulgaria: geodynamic inferences. J. Balkan Geophys. Soc. 3, 13–19.
Sun, W., Jiang, J., Dai, L., Hu, H., Wang, M., Qi, Y., Li, H., 2021. Electrical properties of dry polycrystalline olivine mixed with various chromite contents: Implications for the high conductivity anomalies in subduction zones. Geosci. Front. 12 (5), 101178.
Swain, G., Barovich, K., Hand, M., Ferris, G., Schwarz, M., 2008. Petrogenesis of the St Peter Suite, southern Australia: Arc magmatism and Proterozoic crustal growth of the South Australian Craton. Precambrian Res. 166 (1–4), 283–296. https://doi.org/10.1016/j.precamres.2007.07.028.
Thiel, S., Heinson, G., 2010. Crustal imaging of a mobile belt using magnetotellurics: an example of the Fowler Domain in South Australia. J. Geophys. Res. Solid Earth 115, B06102. https://doi.org/10.1029/2009JB006698.
Thomas, S.M., Koch-Müller, M., Reichart, P., Rhede, D., Thomas, R., Wirth, R., Matsyuk, S., 2009. IR calibrations for water determination in olivine, r-GeO 2, and SiO 2 polymorphs. Phys. Chem. Miner. 36 (9), 489–509.
Tullis, J., Yund, R., Farver, J., 1996. Deformation-enhanced fluid distribution in feldspar aggregates and implications for ductile shear zones. Geology 24 (1), 63–66.
Unsworth, M.J., Jones, A.G., Wei, W., Marquis, G., Gokarn, S.G., Spratt, J.E., Bedrosian, P., Booker, J., Leshou, C., Clarke, G., Shenghui, L., Chanhong, L., Ming, D., Sheng, J., Solon, K., Handong, T., Ledo, J., Roberts, B., 2005. Crustal rheology of the Himalaya and Southern Tibet inferred from magnetotelluric data. Nature 438 (7064), 78–81. https://doi.org/10.1038/nature04154.
Van Leeuwen, A.T.D.V., Morrissey, L.J., Raimondo, T., Hand, M., 2022. Prolonged high thermal gradient metamorphism in the Curnamona Province, south-Central Australia, during the latter stages of Nuna assembly. Precambrian Res. 378, 106775. https://doi.org/10.1016/j.precamres.2022.106775.
Wang, D., Li, H., Yi, L., Matsuzaki, T., Yoshino, T., 2010. Anisotropy of synthetic quartz electrical conductivity at high pressure and temperature. J. Geophys. Res. Solid Earth 115, B09211.
Wang, D., Guo, Y., Yu, Y., Karato, S., 2012. Electrical conductivity of amphibole-bearing rocks: influence of dehydration. Contrib. Mineral. Petrol. 164 (1), 17–25. https://doi.org/10.1007/s00410-012-0722-z.
Wang, D., Yu, Y., Zhou, Y., 2014a. Electrical conductivity anisotropy in alkali feldspar at high temperature and pressure. High Pressure Res. 34 (3), 297–308.
Wang, X., Zhang, G., Fang, H., Luo, W., Zhang, W., Zhong, Q., Cai, X., Luo, H., 2014b. Crust and upper mantle resistivity structure at middle section of Longmenshan, eastern Tibetan plateau. Tectonophysics 619, 143–148.
Wang, Q., Hawkesworth, C.J., Wyman, D., Chung, S.L., Wu, F.Y., Li, X.H., Li, Z.X., Gou, G.N., Zhang, X.Z., Tang, G.J., Dong, Y.H., 2016. Pliocene-Quaternary crustal melting in central and northern Tibet and insights into crustal flow. Nat. Commun. 7 (1), 1–11.
Winter, J.D., 2013. Principles of Igneous and Metamorphic Petrology. Pearson Education, pp. 392–393.
Wolf, M.B., Wyllie, P.J., 1994. Dehydration-melting of amphibolite at 10 kbar: the effects of temperature and time. Contrib. Mineral. Petrol. 115 (4), 369–383. https://doi.org/10.1007/BF00320972.
Xu, S., Unsworth, M.J., Hu, X., Mooney, W.D., 2019. Magnetotelluric evidence for asymmetric simple shear extension and lithospheric thinning in South China. J. Geophys. Res. Solid Earth 124 (1), 104–124.
Yang, X., 2012. Orientation-related electrical conductivity of hydrous olivine, clinopyroxene and plagioclase and implications for the structure of the lower continental crust and uppermost mantle. Earth Planet. Sci. Lett. 317, 241–250.
Yang, X., Keppler, H., McCammon, C., Ni, H., 2012. Electrical conductivity of orthopyroxene and plagioclase in the lower crust. Contrib. Mineral. Petrol. 163 (1), 33–48.
Yin, C., Zhang, B., Han, B.F., Zhang, J., Wang, Y., Ai, S., 2017. Structural analysis and deformation characteristics of the Yingba metamorphic core complex, northwestern margin of the North China craton, NE Asia. J. Struct. Geol. 94, 195–212. https://doi.org/10.1016/j.jsg.2016.11.011.
Yoshino, T., 2010. Laboratory electrical conductivity measurement of mantle minerals. Surv. Geophys. 31 (2), 163–206.